Available online at www.sciencedirect.com

ScienceDirect

International Journal of Solids and Structures 45 (2008) 3375–3391

INTERNATIONAL JOURNAL OF SOLIDS AND STRUCTURES

www.elsevier.com/locate/ijsolstr

A numerical method for rapid estimation of drawbead restraining force based on non-linear, anisotropic constitutive equations

M.G. Lee [a], K. Chung [b], R.H. Wagoner [c], Y.T. Keum [d,*]

[a] *Ferrous Alloy Research Group, Korea Institute of Machinery & Materials, 66 Sangnam, Kyungnam, 641-010, South Korea*
[b] *School of Materials Science and Engineering, ITRC, Seoul National University, Seoul 151-742, South Korea*
[c] *Department of Materials Science and Engineering, The Ohio State University, 2041 College Road, Columbus, OH 43210, USA*
[d] *Division of Mechanical Engineering, Hanyang University, 17 Haengdang-Tong, Sungdong-Ku, Seoul 133-791, South Korea*

Received 18 May 2007; received in revised form 22 January 2008
Available online 15 February 2008

Abstract

Numerical procedures to predict drawbead restraining forces (DBRF) were developed based on the semi-analytical (non-finite-element) hybrid membrane/bending method. The section forces were derived by equating the work to pull sheet material through the drawbead to the work required to bend and unbend the sheet along with frictional forces on drawbead radii. As a semi-analytical method, the new approach was especially useful to analyze the effects of various constitutive parameters with less computational cost. The present model could accommodate general non-quadratic anisotropic yield function and non-linear anisotropic hardening under the plane strain condition. Several numerical sensitivity analyses for examining the effects of process parameters and material properties including the Bauschinger effect and the shape of yield surface on DBRF were presented. Finally, the DBRFs of SPCC steel sheet passing a single circular drawbead were predicted and compared with the measurements.

Keywords: Drawbead; DBRF; Hybrid method; Bauschinger effect; Isotropic–kinematic hardening law; Anisotropic yield function

1. Introduction

In sheet metal stamping process, the drawbeads are frequently utilized to restrain the sheet metal from flowing too freely and to control the amount of draw-in into die cavity. In order to increase the prediction capability of drawbead restraining force (DBRF) in an accurate and effective manner, lots of efforts have been made during several decades. For example, Nine (1978, 1982) studied the effects of various stamping parameters on DBRF and proposed a DBRF and bead-exit prestrain at the upper and lower skins of the sheet when

* Corresponding author. Tel.: +82 2 2220 0436; fax: +82 2 2298 6194.
E-mail address: ytkeum@hanyang.ac.kr (Y.T. Keum).

0020-7683/$ - see front matter © 2008 Elsevier Ltd. All rights reserved.
doi:10.1016/j.ijsolstr.2008.02.008

a circular drawbead is employed in a binder-holding process. Wang (1982) presented a mathematical model for circular drawbead considering bending, sliding with friction and unbending of sheet materials. Levy (1983) added the anisotropy and strain rate dependence of sheet materials in the old models. The most frequently utilized drawbead model up to now was derived by Stoughton (1988) based on the equivalence of work required to pull the sheet through the drawbead to the work required to bend and straighten the sheet and overcome the frictional forces in sliding over the bead radii. This model, to provide finite-element modeling with accurate estimate of the DBRF, thoroughly investigated the effects of drawbead depth, strain rate, bending on the DBRF and binder hold-down force.

Continuous studies on the drawbeads have been emerged especially with the rapid progress of computational methods including finite-element method. Wang and Shah (1991) evaluated the effects of drawbead dimensions and friction coefficients. Demeri (1993) assessed the influence of material properties, drawbead penetration, and lubricants on the sheet flow. Direct simulations using finite-element analysis were performed to predict DBRF and it was reported that a two-dimensional finite-element simulation was able to provide an accurate enough prediction (Sunaga et al., 1996). Cao and Boyce (1993) showed that the restraining force reaches its steady state when a part of the sheet is pulled entirely through the drawbead with their finite-element simulations. More recently, Keum et al. (2001) proposed expert drawbead model which provides the drawing characteristics of the drawbead used in the finite-element analysis of sheet metal forming process to overcome the limitations of previous equivalent drawbead model positioned in the direction of normal to the sheet movement.

Although the previous drawbead models showed reasonable prediction capabilities for the DBRF, they still have some limitations. For example, Stoughton's early model (1988) used simplified constitutive laws such as symmetrical properties on the tension and compression and normal anisotropic yield condition to obtain analytical forms of solutions for the DBRF. Also, the material is assumed to be work-hardened to a strain proportional to the average strain through the thickness in the simplified analytical model. Another theoretical model (Chen and Tszeng, 1998) to calculate the restraining force produced by the drawbead also made simplifying assumptions on the material behavior. Here, they assumed that the material is isotropic rigid–plastic and the Bauschinger effect during the cyclic bending and unbending process was neglected. However, when the material elements undergo non-monotonous deformations, the simple hardening law such as isotropic hardening might not be so effective, even though deformations are approximately proportional. During the reverse loading, material elements usually demonstrate the Bauschinger effect, which is related to the translation of the yield stress surface. Assuming the initial yield stress surface to translate in the stress field without changing its shape and size during plastic deformation is another way to simplify the evolution of the yield stress surface: kinematic hardening proposed by Prager (1956) and Ziegler (1959). In order to describe the expansion and translation of the yield stress surface during plastic deformation, the combination types of the isotropic and kinematic hardening have been also commonly used (Chaboche, 1986; Chung et al., 2005; Geng and Wagoner, 2002). For example, Chun et al. (2002) compared the springback of sheet metals passing draw bead for various material models and concluded that the Bauschinger effect should be properly modeled to give good prediction capability. Besides the hardening law, the yield function which is essential to describe accurate anisotropic behavior of sheet materials should be properly utilized. Recent studies on the non-quadratic anisotropic yield function are well presented for the necessity of more advanced yield surfaces especially for the non-ferrous materials.

Although finite-element method with higher order element such as 3D shell element has been successfully used to predict DBRF with great accuracy, it usually takes much time and cost in the design stage. As an alternate method to save computational expense with reasonable accuracy, a numerical procedure based on the semi-analytical hybrid membrane/bending method which superposes bending effect onto membrane solution has been developed and utilized. For example, similar numerical methods to reduce the computational cost for the springback of sheet metal forming have been suggested in the previous works (Lee et al., 2007; Yoon et al., 2002). As a non-finite-element approaches, they are especially useful to analyze the effects of various constitutive parameters without spending much CPU time, while reasonable range of accuracy.

Due to the simple geometries of drawbeads adopted in sheet metal forming simulation, the semi-analytical numerical method is applied in the present paper. The section forces are derived by the energy equivalence suggested by Stoughton. The sensitivity (parametric) tests are presented for the process parameters and mate-

rial properties. In terms of process parameters, the effects of friction by varying Coulomb friction coefficient and drawbead depth on the DBRF are investigated. In terms of material properties, three different hardening models including (pure) isotropic, (pure) kinematic and non-linear isotropic–kinematic hardening based on Chaboche model and shape of yield function are chosen for the parametric studies. As for the yield function, the Yld2000-2d originally proposed by Barlat et al. (2003) is used to represent the general shape of yield criteria for different structure of metals. Besides the parametric studies, the predicted DBRFs on SPCC steel are compared with measurements for the single circular drawbead.

2. Theory

In the present numerical scheme, the solutions of bending and unbending are superposed onto those of membrane: hybrid method. Under this scheme, the tangential strain is the linear sum of symmetrical bending strain and uniform stretching strain through the thickness. The drawbead adopted in the present paper is circular shape and restraining forces for the membrane solution can be derived in a straight manner without the aid of finite-element calculation unlikely as done in the previous works (Pourboghrat and Chu, 1995; Pourboghrat et al., 1998). As for the constitutive behavior of materials, the combined non-linear isotropic–kinematic hardening is applied (Chung et al., 2005). Therefore, the numerical scheme is inevitably needed to calculate solutions, which satisfy the equilibrium condition at all material points.

2.1. Kinematics

In the simulation of the drawbead test shown in Fig. 1, the tensile force distribution is determined in terms of the material properties, the drawbead geometry and the friction. Then, for every time increment, the length of the central line in each element is determined such that the resulting cross-sectional tensile force satisfies the equilibrium force distribution along the sample.

The tangential strain distribution due to the bending with the applied tension is calculated by sectioning the thickness into N equal-sized layers for each element discretized along the sheet material having an initial area A_0 (Lee et al., 2007). Tangential strains are calculated under the kinematic assumption that the plane section remains plane called as the Kirchoff–Love theory after bending and unbending with tension. This assumption is equivalent to the negligible through-the-thickness shear strains and was validated by the earlier work by Choudhry and Lee (1994). In Fig. 2, the current thickness of the ℓth layer is calculated by applying following recursive equations from the middle layer under the incompressibility assumption:

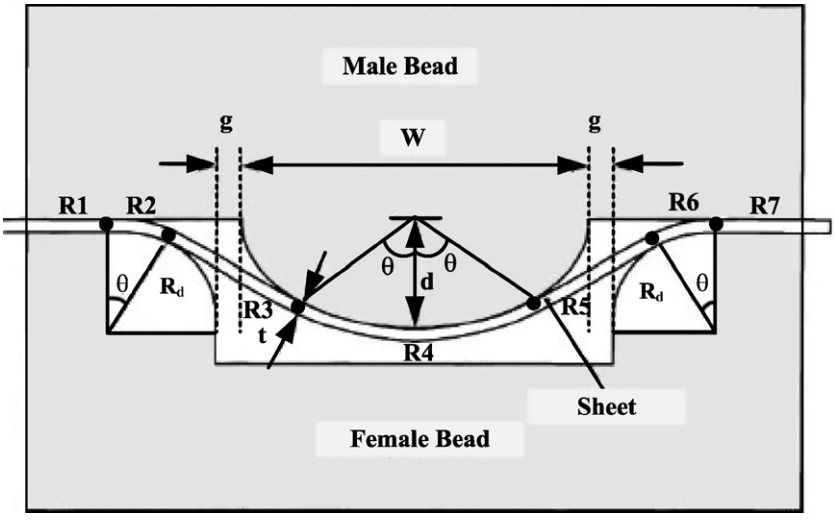

Fig. 1. Section view of a single circular drawbead with geometrical parameters.

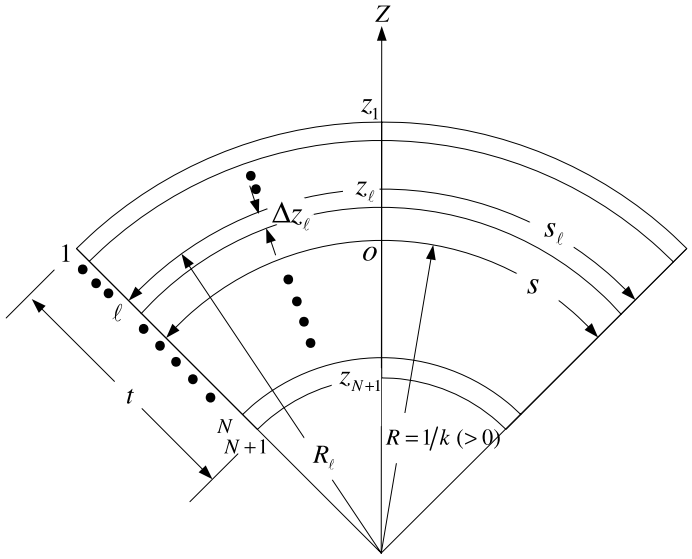

Fig. 2. Definition of N-layers through the thickness.

$$\Delta z_{\ell-1} = \sqrt{R_\ell + 2\frac{R}{S}\frac{A_0}{N}} - R_\ell \tag{1}$$

for the layers above the center line and

$$\Delta z_\ell = R_\ell - \sqrt{R_\ell - 2\frac{R}{S}\frac{A_0}{N}} \tag{2}$$

for the layers below the center line. Here, $R\left(=\frac{1}{\kappa}, \kappa \text{ is curvature}\right)$ and S are the current radius of curvature and length of the centerline, respectively. Eqs. (1) and (2) correspond to the positive bending in which the outer fiber in Fig. 2 is stretched, while inner fiber is compressed. For the negative bending Eq. (1) holds for $\Delta z_{\ell-1}$ above the central line and Eq. (2) holds for Δz_ℓ below the central line. Note that radius of curvature is obtained considering the position of the element along the tool geometry and therefore, $R = R_d + t/2$ in the current drawbead problem shown in Fig. 1.

The discrete tangential strain increment of each layer is calculated by considering the current length and plane strain condition

$$\Delta \varepsilon_{ps,\ell} = \ell n\left(\frac{S_\ell}{{}^0S_\ell}\right) \tag{3}$$

where ${}^0S_l$ is the length of the ℓth layer at the previous time step and $S_\ell = (1 + \kappa z_\ell)\ S$ is its current length.

Applying the constitutive equations described in the later section and Eqs. (1) and (2), the tangential section force is calculated as following.

$$T = \sum_{\ell=1}^{N} \langle \sigma(z_\ell) \rangle \cdot \Delta z_\ell \cdot W \tag{4}$$

where W is the width of the thin sheet and $\langle \sigma(z_\ell) \rangle = \frac{\sigma(z_\ell)+\sigma(z_{\ell+1})}{2}$ is averaged stress between two neighboring segments. Note that the resultant force is determined by the current radius of curvature R and length of the centerline S.

2.2. Distribution of forces along the drawbead

With a sectional geometry of circular drawbead and a finally formed sheet shown in Fig. 1, the drawbead restraining force (DBRF) is derived by equating the work required to pull the sheet through the drawbead to

the work required to bend and straighten the sheet and to overcome the frictional forces in sliding over the cylindrical drawbead radius as done by the previous works Stoughton (1988) and Keum et al. (2001).

First, the angle of drawbead contact between the sheet and drawbead edge radius is given by considering the geometry of circular drawbead.

$$\theta = \tan^{-1}\left(q\frac{((1-p)^2 + p(2-p)(1-q^2))^{1/2} - 1 + p}{(1-q^2)}\right) \tag{5}$$

where $p = \frac{d}{(2R_d+t)}$ is penetration with drawbead depth d, and $q = \frac{(2R_d+t)}{(2R_d+g)}$ is the fit of drawbead with drawbead gap g.

As the sheet material is flowing from region R1 to region R7, the restraining force is accumulated by bending and friction. The force at region R1 is increased by the blank holder force and friction between sheet and blank holder. When the sheet material arrives at the entrance of region R2, the material experiences bending and the additional bending force is accumulated. Therefore, the material element with length ${}^0S$ under the blank holder force T_{BHF} takes up a new central line length S as soon as it enters region R2 under the tension and bending moment. Since R (by the tool radius and current sheet thickness) and T_{BHF} are prescribed, the new S is determined from Eq. (4) along with the stress distribution after extension and bending. Therefore, the plastic work increment rate associated with the material deformation becomes (Lee et al., 2007)

$$\frac{dW}{dt} = \left[\iiint (\sigma \cdot d\varepsilon)dV\Big|_{\text{under tension } T_{BHF} \text{ and bending}} - \iiint (\sigma \cdot d\varepsilon)dV\Big|_{\text{under tension } T_{BHF}}\right] \cdot \left(\frac{v}{{}^0S}\right) \tag{6}$$

where v is the velocity of material movement ${}^0S/v$ and is the time duration of the movement. The increment of the tensile force $\Delta T_{2,B}$ at the entrance of region R2 is obtained by equating Eq. (6) with the work increment rate, $\Delta T_{2,B} \cdot v$ by external forces applied on the strip. Therefore, $\Delta T_{2,B}$ is approximated as

$$\Delta T_{2,B} = \left[\iiint (\sigma \cdot d\varepsilon)dV\Big|_{\text{under tension } T_{BHF} \text{ and bending}} - \iiint (\sigma \cdot d\varepsilon)dV\Big|_{\text{under tension } T_{BHF}}\right] \cdot W \tag{7}$$

During the sliding on the tool surface in the region R2, the force is increased by the resistance by the friction between sheet material and tool surface. Here, the sheet material contacting with the tool is equally divided into n subsections. The force due to the friction at the kth section along the region R2, T_2^k is

$$T_2^k = (T_{BHF} + \Delta T_{2,B}) \cdot \exp\{\mu \cdot (k-1) \cdot \Delta\theta\}, \quad k = 1, \ldots, n+1 \tag{8}$$

where μ and $\Delta\theta$ are the friction coefficient and the incremental angle the sheet slides on the drawbead surface, respectively.

In region R3, the restraining force instantaneously increases at the entrance of the region R3 to overcome the resistance associated with the complete unbending of the material. Therefore, as similarly done for $T_{2,B}$,

$$\Delta T_{3,UB} = \left[\iiint (\sigma \cdot d\varepsilon)dV\Big|_{\text{under tension } T_2^{n+1}} - \iiint (\sigma \cdot d\varepsilon)dV\Big|_{\text{under tension } T_2^{n+1} \text{ and bending}}\right] \cdot W \tag{9}$$

and

$$T_3 = T_2^{n+1} + \Delta T_{3,UB} \tag{10}$$

The increase of the restraining force is repeated as the sheet material travels along the drawbead surface and the restraining forces for other regions can be obtained by the similar procedure described above.

As proposed in the previous works by Stoughton (1988) and Keum et al. (2001), the elastic force due to the initial elastic displacement (δ) during the die closing is added at the first and last points of contact of the center drawbead to the forces due to the bending and the friction. The elastic force (F_e) is calculated by applying the theory of elastic beam bending (from the solution of simply supported beam with deflection δ),

$$F_e = \frac{2Ew\delta t_0^3}{(2R_d + g)} \tag{11}$$

where $\delta = \min\left(d, 2(2R_d + t_0)\frac{R_d\sigma_Y}{t_0 E}\right)$, E is Young's modulus, t_0 is initial sheet thickness, and σ_Y is yield stress of the sheet.

2.3. Constitutive equations

Under the plane strain assumption for a thin shell, the strain components have the following relationship by the additive decomposition,

$$d\varepsilon_2 = d\varepsilon_2^e + d\varepsilon_2^p = 0 \tag{12}$$

where superscripts e and p represent elastic and plastic components, respectively. The subscript 2 shows the component of strain along which the strain is constrained. When the plane stress condition is further imposed for a thin sheet (that is, the normal compressive stresses are neglected), the stress state is generally not proportional under the elasto-plastic formulation, as schematically shown in Fig. 3(a). As a way

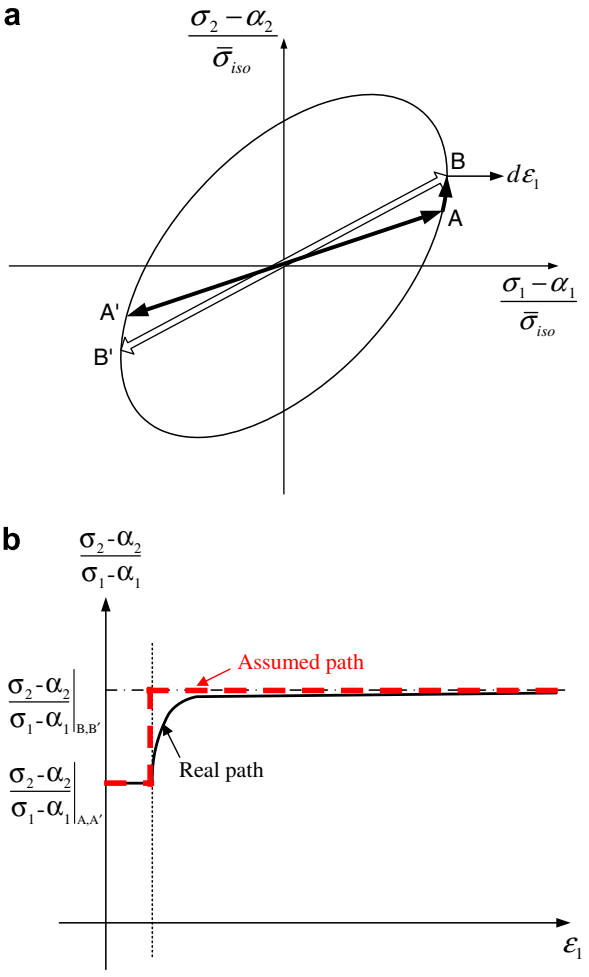

Fig. 3. (a) Stress state of a thin sheet in the plane-stress stress field under the plane strain deformation in elasto-plasticity and (b) rapid development of the proportional stress state during the initial plastic deformation (Lee et al., 2007).

to achieve the proportionality in loading for the simple analysis here, the loading in Fig. 3(a) was approximated to that in Fig. 3(b): within the yield surface, the stress is proportional under the condition, $d\varepsilon_2 = d\varepsilon_2^e = 0$, and as soon as the stress reaches the yield surface, the stress is proportional under the condition, $d\varepsilon_2^p = 0$.

By the linear elasticity,

$$d\sigma_{ps} = E^{ps}(d\varepsilon_{ps} - d\varepsilon_{ps}^p) \tag{13}$$

where $E^{ps} = \frac{E}{1-v^2}$. Here, the 'ps' means the components of the plane strain deformation, while E and v are Young's modulus and Poisson ratio of elasticity, respectively. By applying the modified plastic work equivalence principle for the isotropic–kinematic hardening law (Chung et al., 2005),

$$\bar{\sigma}_{iso} d\bar{\varepsilon} = |\sigma_{ps} - \alpha_{ps}| \cdot |d\varepsilon_{ps}^p| \tag{14}$$

where the upper bar is used for equivalent values and subscript 'iso' means the isotropic hardening (therefore, $\bar{\sigma}_{iso}$ represents the current size of the expanding yield surface), while α_{ps} is the back stress which represents the translation of the initial yield surface. When the yield function is specified, the ratio β between $|\sigma_{ps} - \alpha_{ps}|$ and $\bar{\sigma}_{iso}$ is determined by calculating the stress point on the yield surface, which satisfies the plane strain condition ($d\varepsilon_2^p = 0$). Therefore, Eq. (14) leads to

$$|\sigma_{ps} - \alpha_{ps}| = \beta\bar{\sigma}_{iso}, |d\varepsilon_{ps}^p| = \frac{1}{\beta} d\bar{\varepsilon} \tag{15}$$

For the evolution of the back stress, the combination type isotropic–kinematic hardening law based on the Chaboche model (Chaboche, 1986) under the plane strain condition is adopted in the paper:

$$d\alpha_{ps} = C_1 |d\varepsilon_{ps}^p| \frac{\beta^2(\sigma_{ps} - \alpha_{ps})}{|\sigma_{ps} - \alpha_{ps}|} - C_2 \alpha_{ps} \beta |d\varepsilon_{ps}^p| \tag{16}$$

where C_1 and C_2 are material parameters measured at the reference state which is the uni-axial tension state in this work.

The linear decomposition of the total hardening into isotropic and kinematic part can be assumed as following:

$$\bar{\sigma} = \bar{\sigma}_{iso} + \bar{\sigma}_{kine} = \{\bar{\sigma}_0 + \xi q(1 - e^{-b\bar{\varepsilon}})\} + (1 - \xi) q(1 - e^{-b\bar{\varepsilon}}) \tag{17}$$

where the material parameter ξ is used as a ratio between the size change of yield surface by isotropic hardening and translation of yield surface by kinematic hardening. Therefore, the above equation efficiently can represent pure isotropic ($\xi = 1$), combined isotropic–kinematic hardening ($0 < \xi < 1$), and pure kinematic hardening ($\xi = 1$). Note that ξ is generally a function of $\bar{\varepsilon}$.

For the evolution of back stress, the Chaboche type non-linear kinematic hardening rule becomes, for the uni-axial tensile case,

$$\frac{d\alpha}{d\varepsilon^p} = C_1 - C_2 \alpha \tag{18}$$

Integrating Eq. (18) and comparing it with the kinematic part of hardening in Eq. (17) gives,

$$C_1 = b \text{ and } C_1 = (1 - \xi)\text{qb} \tag{19}$$

Since the parameter ξ determines the early re-yielding when the loading direction is reversed, this parameter is equivalent to the Bauschinger ratio.

The hardening parameters $\bar{\sigma}_{iso}(\bar{\varepsilon})$ for isotropic hardening and C_1 and C_2 for the kinematic hardening are characterized from the continuous tension–compression (or compression–tension) uni-axial tests with several pre-strains. From the measured data, initially the isotropic hardening data is separated from the total hardening data. Then, the two kinematic hardening parameters which are assumed to be constants in this work are obtained by the fitting the equation $\bar{\alpha} = \frac{C_1}{C_2}(1 - e^{-c_2\bar{\varepsilon}})$ for the rest portion of the hardening. Note that C_1 and C_2 are the functions of $\bar{\varepsilon}$ in general and the value β is obtained from the prescribed yield surface described in the following Section 2.4.

2.4. Anisotropic yield stress function: Yld2000-2d

In order to describe the initial anisotropic yield stress surface, the yield function proposed by Barlat et al. (2003) for the plane stress state is considered. The anisotropic yield function is defined as

$$f = \frac{\phi' + \phi''}{2} \tag{20}$$

where $\phi' = |X'_1 - X'_2|^m$, $\phi'' = |2X''_2 + X''_1|^m + |2X''_1 + X''_2|^m$.

Here, f is the sum of two isotropic functions, which are symmetric with respect to X_1 and X_2. In the above equation, X_1 and X_2 are the principal values of the matrices, $\mathbf{X}'$ and $\mathbf{X}''$, whose components are obtained from the following linear transformation of the Cauchy stress ($\boldsymbol{\sigma}$) and the deviatoric Cauchy stress ($\boldsymbol{\sigma}'$), respectively:

$$\mathbf{X}' = \mathbf{C}'\boldsymbol{\sigma}' = \mathbf{C}'\mathbf{T}\boldsymbol{\sigma} = \mathbf{L}'\boldsymbol{\sigma} \tag{21}$$

and

$$\mathbf{X}'' = \mathbf{C}''\boldsymbol{\sigma}' = \mathbf{C}''\mathbf{T}\boldsymbol{\sigma} = \mathbf{L}''\boldsymbol{\sigma} \tag{22}$$

where

$$\begin{bmatrix} L'_{11} \\ L'_{12} \\ L'_{21} \\ L'_{22} \\ L'_{66} \end{bmatrix} = \begin{bmatrix} 2/3 & 0 & 0 \\ -1/3 & 0 & 0 \\ 0 & -1/3 & 0 \\ 0 & 2/3 & 0 \\ 0 & 0 & 1 \end{bmatrix} \begin{bmatrix} \alpha_1 \\ \alpha_2 \\ \alpha_7 \end{bmatrix} \text{ and } \begin{bmatrix} L''_{11} \\ L''_{12} \\ L''_{21} \\ L''_{22} \\ L''_{66} \end{bmatrix} = \frac{1}{9} \begin{bmatrix} -2 & 2 & 8 & -2 & 0 \\ 1 & -4 & -4 & 4 & 0 \\ 4 & -4 & -4 & 1 & 0 \\ -2 & 8 & 2 & -2 & 0 \\ 0 & 0 & 0 & 0 & 1 \end{bmatrix} \begin{bmatrix} \alpha_3 \\ \alpha_4 \\ \alpha_5 \\ \alpha_6 \\ \alpha_8 \end{bmatrix} \tag{23}$$

where the eight coefficients, α_1–α_8 are anisotropic parameters which are obtained by the uni-axial tensile tests with different directions and bi-axial test. However, when only seven coefficients are needed to account for the seven input data for such as σ_0, σ_{45}, σ_{90}, r_0, r_{45}, r_{90} and r_b, it may be assumed that $\alpha_3 = \alpha_6$ (therefore, $L''_{12} = L''_{21}$) or $\alpha_4 = \alpha_5$ (therefore $L''_{11} = L''_{22}$). The detailed characterization method for the yield stress surface and hardening data is referred to the previous works (Lee et al., 2005a,b).

2.5. Numerical procedure

To calculate the stress expressed in Eq. (4), the numerical implementation follows the general procedure of update algorithm using the elasto-plastic constitutive equations. First, the discrete tangential strain increment is calculated using the drawbead geometry as described in Section 2.1 under the assumption of membrane strain distribution. Next, the stress and other variables, such as equivalent plastic strain and back-stress, are updated. The predictor–corrector scheme based on the Newton–Raphson method is used to solve the unknown-increment of equivalent plastic strain. Finally, the equilibrium is checked by equating tangential force derived in Eq. (4) with the prescribed tensile force distribution, which leads to simultaneous non-linear equations for the membrane strain distribution. Here, the bi-section method was utilized to find the solutions iteratively, in which a few number of iterations are needed for the solution in most cases. Note that the tensile forces in the whole regions are numerically pre-determined with material properties and tool geometry. The summary of the numerical procedure applied in the paper is schematically shown in Fig. 4.

3. Results and discussion

3.1. Numerical parametric tests

In order to validate the developed semi-analytical hybrid procedure, numerical sensitivity tests have been performed for the effects of various parameters such as process and materials on the drawbead restraining forces. In terms of process parameters, the friction and the amount of drawbead penetration are investigated. For the material effects, the type of hardening law and the shape of yield surface are chosen for the sensitivity tests.

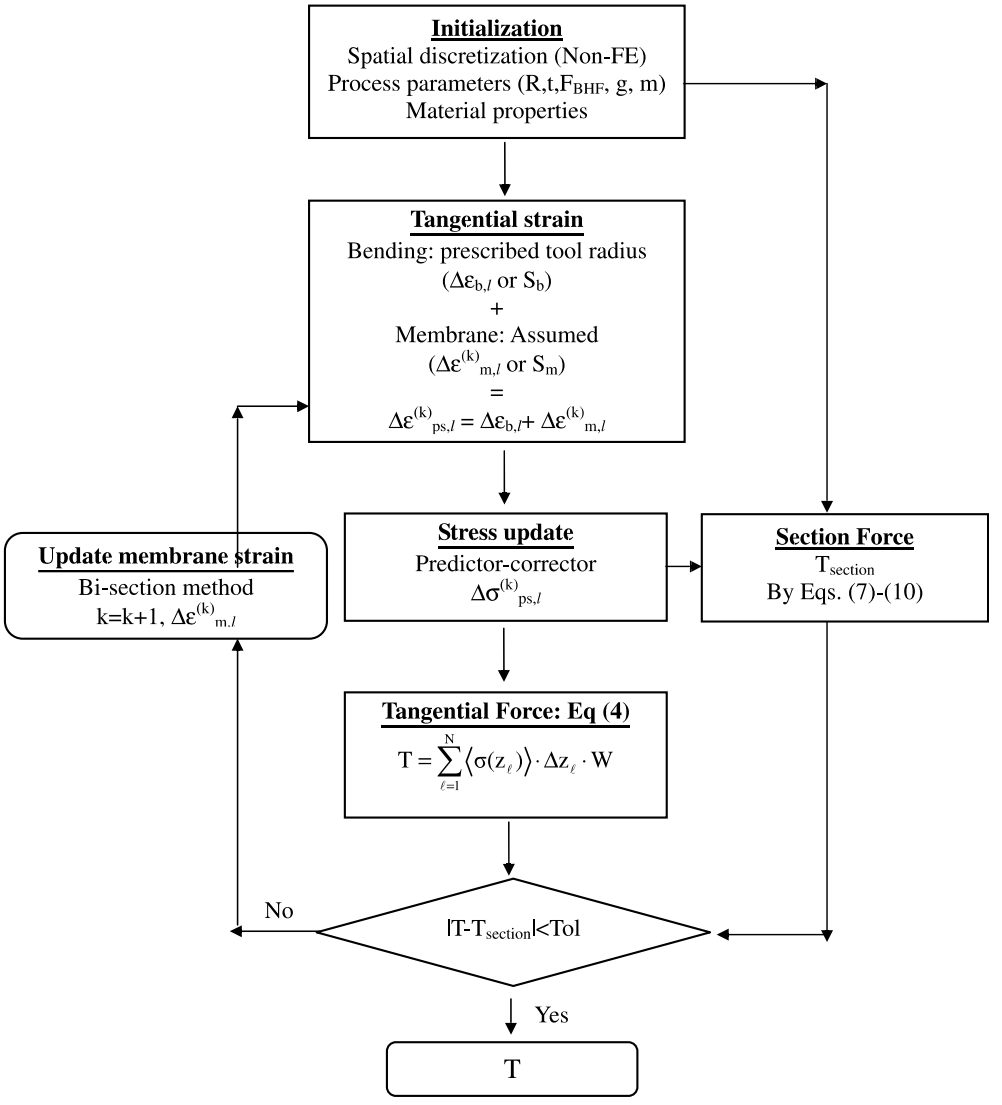

Fig. 4. The hybrid numerical scheme.

The reference conditions employed in the sensitivity tests are as followings:

- *Voce type hardening equation*, $\bar{\sigma} = \bar{\sigma}_0 + q(1 - e^{-b\bar{\varepsilon}})$

  $\bar{\sigma}_0 = 166.2$ MPa, $q = 215.8$ MPa, $b = 8.9$.

- *Isotropic hardening law.*
- *Isotropic yield function*: α_1–$\alpha_8 = 1$.
- *Yield potential exponent*; $m = 8$.
- *Young's modulus*; $E = 70$ GPa, *Poisson's ratio*; $v = 0.33$.
- *Radius of drawbead*; $R_d = 5.5$ mm.
- *Sheet thickness*; $t = 0.81$ mm.
- *Width of sheet*; $W = 50$ mm.
- *Drawbead gap*; $g = t + 0.08$ mm.
- *Bead depth*; $d = 2R_d + t$.
- *Coulomb friction coefficient*; $\mu = 0.15$.

The sheet is divided into 20 subsections through the thickness and 200 increments are utilized for the bending and unbending steps.

3.1.1. Effect of process

Fig. 5 shows DBRF associated with various Coulomb friction coefficients in the range between 0 and 0.2 for the reference condition described above. The DBRF increases as the friction coefficient increases. This result is readily expected because the higher friction increases resistance of sliding sheet element on the bead radius. Fig. 5 also shows that the curve fitting with an exponential function represents well the relation between DBRF and friction coefficient. This is because the tension force increases exponentially as the material travels on the drawbead as shown in Eq. (8).

Fig. 6 shows DBRF as a function of drawbead depth d. As the drawbead depth increases, the angle of contact between sheet material and drawbead radius increases, as calculated by Eq. (5). This is explained by the fact that the restraining force increases as a function of contact angle as shown in Eq. (8). Also, a solid line is the fitted curve by the 4 parameter sigmoid function which represents S shape increase. The contact angle with respect to the drawbead penetration is also presented in Fig. 7, which shows consistency in the shape of fitted curve with the same type of fitting curve.

3.1.2. Effect of materials

The continuum plasticity consists of the description of elastic region by the yield function and its evolution by the hardening law along with elastic properties such as Young's modulus and Poisson's ratio. In contrast to

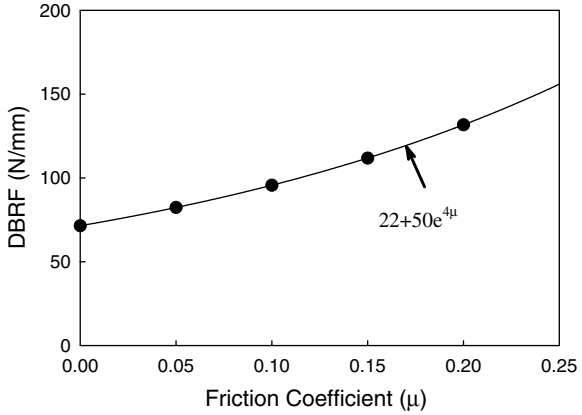

Fig. 5. Draw bead restraining forces (DBRF) with respect to the friction coefficient (μ). ($d = 11.81$, $R_d = 5.5$ mm, $t = 0.81$ mm, $g = 0.89$ mm.)

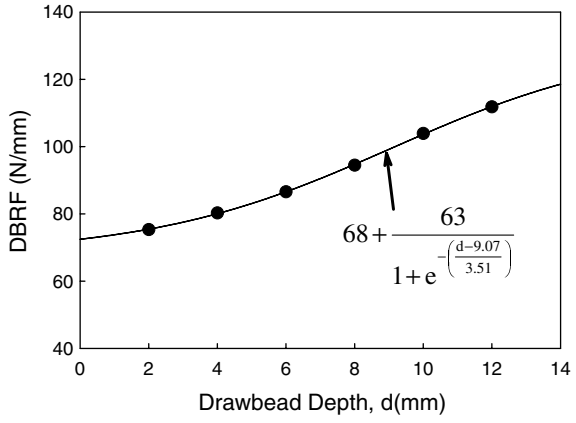

Fig. 6. Draw bead restraining forces (DBRF) with respect to the drawbead depth. ($R_d = 5.5$ mm, $t = 0.81$ mm, $g = 0.89$ mm, $\mu = 0.15$.)

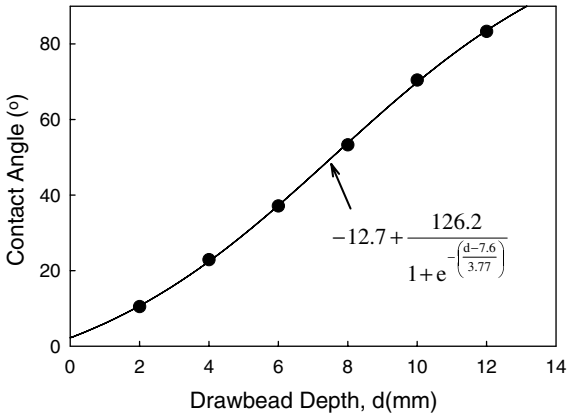

Fig. 7. Contact angle with respect to the drawbead depth. ($R_d = 5.5$ mm, $t = 0.81$ mm, $g = 0.89$ mm, $\mu = 0.15$.)

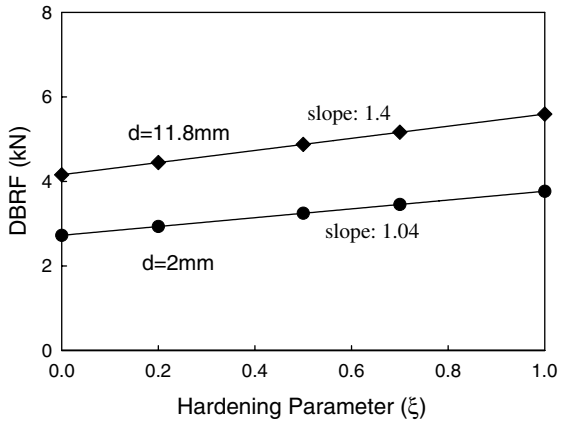

Fig. 8. Draw bead restraining forces (DBRF) with respect to the hardening types.

the analytical model to predict DBRF, advanced constitutive equations are adopted in this paper to represent the material behavior of real metallic material.

Fig. 8 shows the DBRFs associated with various hardening parameters ξ for small draw bead penetration ($d = 2$) and the large bead penetration ($d = 11.8$). In general, the larger DBRFs are predicted as the material parameter ξ approaches 1. That is to say, the maximum DBRF is predicted for the pure isotropic hardening law, while the minimum value is obtained by pure kinematic hardening law. The differences in DBRF between two extreme hardening models are approximately 27% and 26% for two drawbead penetrations, respectively. The figure also shows that the rate of increase of DBRF is linear and the higher rate is observed as the bead penetration increases. In general, the sheet materials utilized for automotive parts are reported to have 50–70% Bauschinger ratio (Lee et al., 2005a,b; Kim et al., 2003). Therefore, the sensitivity results seen in Fig. 8 confirm that the accurate modeling of hardening behavior will play a significant role in predicting the DBRF. The differences in DBRF associated with hardening models can be explained by the stress–strain responses with non-monotonous deformation state. Fig. 9 shows the history of stress–strain curves of the most outer sheet surface ($z = -t/2$) in the region 6 shown in Fig. 1. The most outer surface of the sheet element passing through the region 6 experiences consecutively the bending and unbending processes. As shown in Fig. 9, the stresses of all hardening models have the same value when the sheet undergoes the first bending (monotonic compression). However, when the deformation path is changed by passing the unbending area, the stresses become quite different by the amount of assumed Bauschinger ratio of each hardening type. The differences in the stress significantly affect the amount of additional bending energies. Note that the difference in stress state among hardening models becomes more significant when the sheet element experiences more cyclic deformation. In addition to the tensile

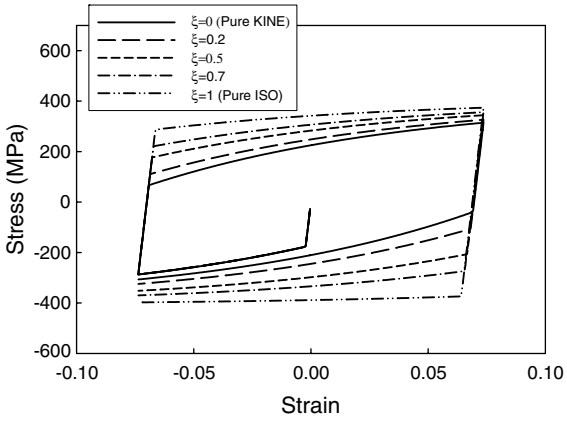

Fig. 9. Stress–strain history of a sheet element at the outer fiber with respect to the hardening type (ξ).

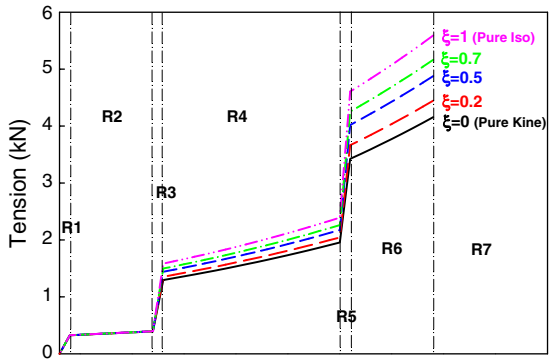

Fig. 10. Effect of hardening type on increase in tension force at each region.

force at the exit of drawbead, the increase in tensile forces in 6 regions with respect to different hardening types are shown in Fig. 10. The figure explicitly shows the increase of tensile force as the material experiences bending, unbending and sliding with friction at the contact regions (regions 2, 4 and 6). Regarding the effect of hardening type, the difference in tension increasingly becomes significant as the material experiences more bending and unbending, as explained in the stress–strain history. Note that there is no difference in tension when the material passes in region 2 in which the material does not experience the path change yet.

Yield surface is another important part of constitutive equations in describing material behavior of metals. Thus, in this paper, the effect of the yield surface on DBRF is investigated. Among the parameters in Yld2000-2d, the exponent m determines the shape of yield surface and can represent from Von Mises yield surface with $m = 2$ to Tresca yield surface with $m =$ infinity. Generally, the exponent 6 for BCC metals and 8 for FCC metals are recommended based on the texture analysis. Here, four exponents $m = 2$, 6, 8, 16 are chosen for the sensitivity tests. The other parameters are set unity so that only isotropic case is considered. Example shapes of Yld200-2d yield functions with different exponents are shown in Fig. 11. Fig. 12 shows the DBRFs associated with different exponents for two drawbead depths. It shows that the DBRF increases linearly as the exponent decreases. The decrease in DBRF can be explained by the relation between the exponent m and parameter β in Eq. (15). As the exponent m decreases, β increases, which results in the increase of stress corresponding to the plane strain state for the same uni-axial hardening behavior.

3.2. Comparison of prediction with measurement

The measured DBRFs of a single circular drawbead with two different conditions are compared with the prediction in this section. The initial size of sheet strip is 45 mm (width) × 300 mm (length). The drawing force

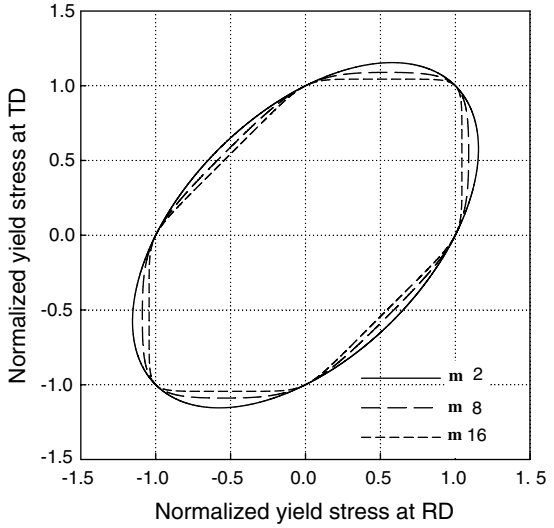

Fig. 11. The yield locus for three different exponents of Yld2000-2d.

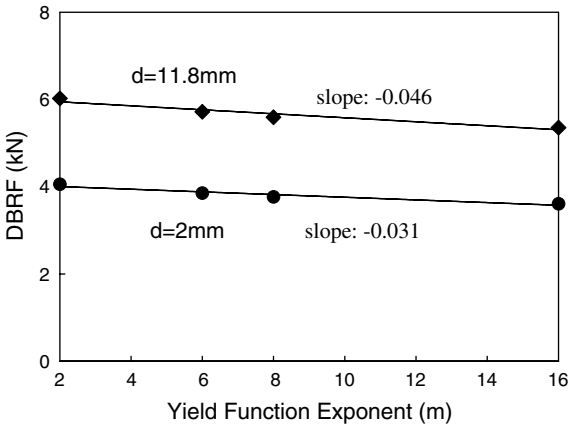

Fig. 12. Draw bead restraining forces (DBRF) with respect to the shape of yield surface.

is measured while the grip clamping an edge of the specimen is pulled out. The friction coefficient was obtained from the Coulomb friction law relating the normal force and frictional force. Using the drawing tests, the frictional force was obtained from the difference between the DBRFs obtained in the fixed drawbead and roller drawbead drawing tests. On the other hand, the normal force is the blank holder force (BHF). The detained experimental procedure can be referred to the previous work by Keum et al. (2001). The material is SPCC steel and two experimental data with different sheet thicknesses and friction coefficients are reproduced for the comparisons.

The hardening behavior of SPCC steel sheet obtained from uni-axial tension tests is fitted by the Voce type equation, as shown in Fig. 13. The elastic properties are $E = 200$ GPa, $v = 0.3$ and the hardening parameters are $\bar{\sigma}_0 = 165$ MPa, $q = 193$ MPa and $b = 12.8$. As for the anisotropic yield surface, six material data including three uni-axial yield stresses, three r-values in the three material directions listed in Table 1 are utilized. Another material data for the balanced-biaxial yield stress normalized by the rolling (0° direction) is assumed unity. The exponent of Yld2000-2d is $m = 6$ to represent BCC metals. The seven anisotropic coefficients of Yld2000-2d described in the previous section, assuming $\alpha_3 = \alpha_6$, are calculated using the Newton–Raphson iteration method and listed in Table 2. The yield surface of SPCC steel normalized by yield stress in the rolling direction is presented in Fig. 14. The figure shows the yield surface of SPCC has round corner with the nature

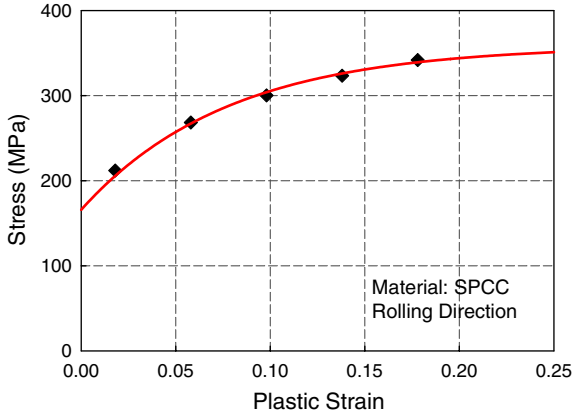

Fig. 13. Stress–strain response for the SPCC steel and its fitting with Voce type hardening equation.

Table 1
Tensile properties of the SPCC steel sheet

Direction (°)	Yield strength (MPa)	UTS (MPa)	Elongation (%)	*r*-value
0	165.0	296.0	45.1	1.80
90	166.7	295.7	43.8	1.97
45	174.3	309.3	40.9	1.14

Table 2
Anisotropic coefficients of Yld2000-2d for SPCC steel sheet

m	α_1	α_2	α_3	α_4	α_5	α_6	α_7	α_8
6	1.06	1.04	1.07	0.96	0.97	1.08	0.97	0.85

of non-quadratic function. The dimensions of circular drawbead are: $R_d = 3.3$ mm (bead radius), $d = 3$ mm (bead height). The calculations by adopting the current hybrid method are performed and compared with the two sets of measurement. In terms of the bead gap, $g = t + 0.2$ mm where t is sheet thickness was used

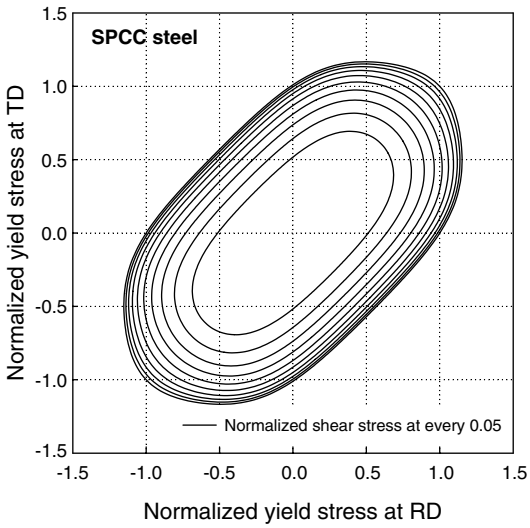

Fig. 14. The calculated yield surface for the SPCC steel.

for the following two examples. In Fig. 15(a), the measured DBRF associated with (lower) BHF = 110 N/mm, $\mu = 0.14$, $t = 0.6$ mm is compared with the simulated results by different hardening models. In addition to the prediction with the current constitutive equations, the equivalent drawbead model originally proposed by Stoughton (1988) and later modified by Keum et al. (2001) was also compared. The explicit form of the equivalent drawbead forces can be referred to their earlier works (for example, Eq. (5) in Keum et al. (2001) was used here to consider the effect of blank holder force on top of the original result by Stoughton (1988)). Note the effective bead radius ($R_{d,eff}$) defined in the work by Stoughton (1988) was used instead of using physical bead radius: $1/R_{d,eff} = \sin(\theta)/R_d$. The hardening parameters for the Stoughton's model are $K = 485.6$ MPa and $n = 0.2$ for the power law type equation $\bar{\sigma} = K\varepsilon^n$. As done in the parametric tests, the pure isotropic hardening and pure kinematic hardening are represented with $\xi = 1.0$ and $\xi = 0$, respectively, in Eq. (17). The figure shows that the results by the pure isotropic hardening and Stoughton's model overestimate measured DBRF, while pure kinematic hardening underestimates. When the pure isotropic model based on the present hybrid model and the Stoughton's equivalent draw bead model are compared, the prediction in the absolute values are similar. The difference between these two models might be due to the different flow equations, yield functions and effective bead radius introduced in the equivalent draw bead model. Since the uni-axial tension/compression data are not available for this material, which are needed to characterize the Bauschinger effect, the best Bauschinger ratio, or ξ is employed from the previously reported value. The value $\xi = 0.6$ shows a good agreement with experimentally measured DBRF. Similar comparisons are made in Fig. 15(b) for different set of measurement with (higher) BHF = 165 N/mm, $\mu = 0.17$, $t = 0.8$ mm. The result is quite similar as that for lower BHF when the Bauschinger ratio is $\xi = 0.6$. The overestimation by the Stoughton's model was

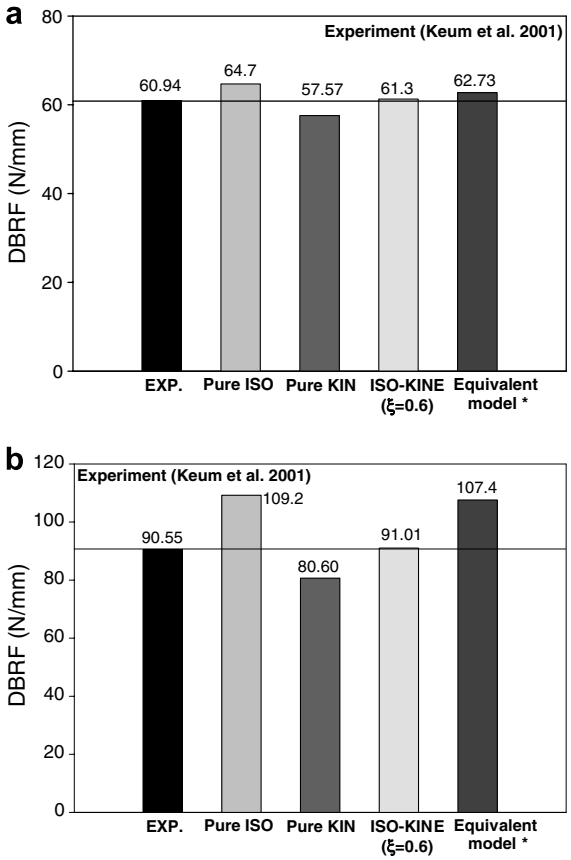

Fig. 15. Comparison of predicted results and measure DBRF; (a) BHF = 110 N/mm, $t = 0.6$, $\mu = 0.14$, $R_d = 3.8$ mm, $d = 3$ mm, (b) BHF = 165 N/mm, $t = 0.8$, $\mu = 0.17$, $R_d = 3.8$ mm, $d = 3$. *Equivalent model is based on the model proposed by Stoughton (1988) and Keum et al. (2001).

expected because it is also based on the isotropic hardening and therefore cannot consider earlier yielding during the reverse bending.

In some previous works (Lee et al., 2005a,b), no significant differences were reported between results predicted from the (pure) isotropic hardening model and combined isotropic–kinematic hardening model in formability and springback of automotive part. The springback of automotive parts is significant in the sidewall curl where the sheet material experiences one consecutive bending and unbending, while the material in the draw bead undergoes multiple process of reverse loading. Fig. 10 supports this for the predicted draw bead restraining force in that the differences in the bead force among various material models are not so significant during the early region but become relatively larger as the material passes the draw bead. Therefore, as the comparisons show, the real DBRFs can be predicted when the constitutive equations which can represent the real anisotropic behavior of sheet material are taken into consideration. Also, it is concluded that the developed numerical method can be successfully used to predict the accurate DBRF without spending much computation cost.

4. Conclusions

(1) Semi-analytic hybrid membrane/bending method based on plane strain state was developed to predict the drawbead restraining force. Since the developed method is not based on the finite-element procedure for the solutions of bending and stretching, it is computationally efficient.
(2) The developed hybrid method can accommodate the combination type isotropic–kinematic hardening law and non-quadratic anisotropic yield function. Thus, the method effectively considers the mechanical behavior of real metallic materials which show Bauschinger effect, transient behavior and significant anisotropy.
(3) Numerical sensitivity tests were carried out by varying process and material parameters. In terms of process effect, the DBRFs as functions of friction coefficient and drawbead depth were calculated. The DBRF increases exponentially as the friction coefficient increases, while shows sigmoid increase as the bead depth increases. In terms of material effects, different hardening models and the shape of yield function were considered in the sensitivity tests. The calculation with (pure) isotropic hardening model resulted in the maximum DBRF, while minimum value was predicted for the (pure) kinematic hardening. The difference in DBRF for the two extreme hardening models was approximately 26%. With increasing exponent of Yld2000-2d the DBRF decreased linearly, which is due to the smaller plane strain stress for larger exponent.
(4) The comparisons between measurements and calculations for the SPCC steel showed that the anisotropic hardening behavior should be considered to precisely predict the DBRF in drawbead simulation. Especially, when the approximate Bauschinger ratio for the steel sheet which was reported in other works is considered, the calculated DBRFs gave good agreement with those of experiments.

Acknowledgements

This work was supported by the Korea Science and Engineering Foundation (KOSEF) through the SRC/ERC Program of MOST/KOSEF (R11-2005-065) and by the National Science Foundation (NSF) (DMI-0355429), which are greatly appreciated.

References

Barlat, F., Brem, J.C., Yoon, J.W., Chung, K., Dick, R.E., Choi, S.H., Pouboghrat, F., Chu, E., Lege, D.J., 2003. Plane stress yield function for aluminum alloy sheets-part 1: theory. Int. J. Plasticity 19, 1297.

Cao, J., Boyce, M.C., 1993. Drawbead penetration as a control element of material flow, SAE paper No. 930517, Sheet Metal and Stamping Symposium, Detroit, USA.

Chaboche, J.L., 1986. Time-independent constitutive theories for cyclic plasticity. Int. J. Plasticity 2, 149.

Chen, K.F., Tszeng, P.C., 1998. An analysis of drawbead restraining force in the stamping process. Int. J. Mach. Tool Manu. 38, 827–842.

Choudhry, S., Lee, J.K., 1994. Dynamic plane-strain finite element simulation of industrial sheet-metal forming processes. Int. J. Mech. Sci. 36, 189–207.

Chun, B.K., Kim, H.Y., Lee, J.K., 2002. Modeling the Bauschinger effect for sheet metals, part II: applications. Int. J. Plasticity 18, 597–616.

Chung, K., Lee, M.G., Kim, D., Kim, C., Wenner, M.L., Barlat, F., 2005. Springback evaluation of automotive sheets based on isotropic–kinematic hardening laws and non-quadratic anisotropic yield functions, Part I: theory. Int. J. Plasticity 21, 861.

Demeri, M.Y., 1993. Drawbeads in sheet metal forming. J. Mater. Eng. Perform. 2, 863.

Geng, L., Wagoner, R.H., 2002. Role of plastic anisotropy and its evolution on springback. Int. J. Mech. Sci. 44, 123.

Keum, Y.T., Kim, J.H., Ghoo, B.Y., 2001. Expert drawbead models for finite element analysis of sheet metal forming processes. Int. J. Solids Struct. 38, 5335.

Kim, D., Lee, M.G., Kim, C., Wenner, M.L., Wagoner, R.H., Barlat, F., Chung, K., 2003. Measurements of anisotropic yielding, Bauschinger and transient behavior of automotive dual-phase steel sheets. Metals Mater. Int. 9, 561.

Lee, M.G., Kim, D., Chung, K., Wagoner, R.H., 2007. Semi-analytic hybrid method to predict springback in 2-D draw bend test. J. Appl. Mech. ASME 74, 1264–1275.

Lee, M.G., Kim, D., Kim, C., Wagoner, R.H., Wenner, ML., Chung, K., 2005a. Springback evaluation of automotive sheets based on isotropic–kinematic hardening laws and non-quadratic anisotropic yield functions, Part II: characterization of material properties. Int. J. Plasticity 21, 883.

Lee, M.G., Kim, D., Kim, C., Wagoner, R.H., Chung, K., 2005b. Springback evaluation of automotive sheets based on isotropic–kinematic hardening laws and non-quadratic anisotropic yield functions, Part III: applications. Int. J. Plasticity 21, 915.

Levy, B.S., 1983. Development of a predictive model for draw bead restraining forces utilizing work of Nine and Wang. J. Appl. Metal. Working 3, 38.

Nine, H.D., 1978. In: Koistinen, D.P., Wang, N.M. (Eds.), Draw-Bead Forces in Sheet Metal Forming, Mechanics of Sheet Metal Forming. Plenum Press, New York.

Nine, H.D., 1982. The applicability of Coulomb's friction law to drawbeads in sheet metal forming. J. Appl. Metal Working 2, 185.

Prager, W., 1956. A new method of analyzing stresses and strains in work hardening plastic solids. J. Appl. Mech. ASME 65, 671.

Pourboghrat, F., Chu, E., 1995. Springback in plane strain stretch/draw sheet forming. Int. J. Mech. Sci. 36, 327.

Pourboghrat, F., Chung, K., Richmond, O., 1998. A hybrid membrane/shell method for rapid estimation of springback in anisotropic sheet metals. ASME J. Appl. Mech. 65, 671.

Stoughton, T.B., 1988. Model of drawbead forces in sheet metal forming. In: Proceedings of the 15th IDDRG, Dearbon, USA, p. 205.

Sunaga, H., Yoneda, K., Makinouchi, A., 1996. Finite element modeling of drawbead in sheet metal forming, Numerical Simulations of 3-D Sheet Metal Forming Process (NUMISHEET'96), Michigan, USA, p. 186.

Wang, N.M., 1982. A mathematical model of drawbead forces in sheet metal forming. J. Appl. Metal. Working 2, 193.

Wang, N.M., Shah, V.C., 1991. Drawbead design and performance. J. Mater. Shaping Tech. 9, 21.

Yoon, J.W., Pourboghrat, F., Chung, K., Yang, D.Y., 2002. Springback prediction for sheet metal forming process using a 3D hybrid membrane/shell method. Int. J. Mech. Sci. 44, 2133.

Ziegler, H., 1959. A modification of Prager's hardening rule. Quart. Appl. Math. 17, 55.